49th AIAA Aerospace Sciences Meeting including the New Horizons Forum and Aerospace Exposition
4 - 7 January 2011, Orlando, Florida

AIAA 2011-228

Fully Coupled Fluid-Structural Interaction of a Transonic Rotor at Near-Stall Conditions Using Detached Eddy Simulation

Xiangying Chen* Hongsik IM† and Ge-Cheng Zha‡
Dept. of Mechanical and Aerospace Engineering
University of Miami
Coral Gables, Florida 33124

Abstract

This paper presents a numerical methodology to study the mechanism of stall flutter at near stall conditions using high fidelity detached eddy simulation (DES) in conjunction with a fully coupled fluid-structural interaction (FSI) model. At near-stall conditions, the flow is highly unsteady due to tip leakage vortex and may induce stall flutter. Such problems often involve shock wave-turbulent boundary layer interaction and flow separation due to rotating stall. In order to capture the possible flutter at near stall conditions, the DES is performed in a single passage domain with circumferential periodicity. The CFD techniques used include: a 5th order WENO scheme with a low diffusion Riemann solver for the inviscid fluxes, a fully conservative 4th order central differencing scheme for the viscous terms, a fully coupled fluid-structural interaction methodology, and a massive parallel procedure. The structural solver employs the efficient and accurate modal approach with five major mode shapes for the rotor blade. The work described herein will lay the foundation for the future work of simulating non-synchronous vibration.

Keywords: Detached eddy simulation; Rotor stall flutter; Fluid-structural interaction

1 Introduction

Transonic flows in turbomachinery are highly non-linear and three dimensional especially at near-stall conditions. The complicated non-linear flow phenomena, including flow induced vibration, flow separation, tip vortices, vortex shedding, shock wave/turbulent boundary layer interactions, make the accurate calculation of unsteady aero-mechanic problems very difficult. The CFD tools used by turbomachinery industry today often fail to detect actual flutter boundary. The primary reason for the inaccurate computation is considered due to the inadequacy of loosely coupled fluid-structural approach and turbulence simulation. The loosely coupled methods can be only formally first-order accurate in time. The turbulence closure techniques used in turbomachinery industry today are almost all based on Reynolds averaged Navier-Stokes(RANS) equations. It is very difficulty, if not impossible, to correctly simulate such complicated flow with RANS motheds which model the entire range of the turbulence scales using a single turbulence model.

In aeroelastic analysis, turbulence modelling is still the bottleneck for handling the complex flows with the unsteady massive separation flows. The early attempt to evaluate turbulence models in aeroelastic

---

[*] Research Associate Professor
[†] PhD. Student
[‡] Associate Professor

applications was made by Srinivasan et al.[1]. Five widely-used turbulence models, namely the Baldwin-Lomax model [2], the Renormalization Group model [3], the half-equation Johnson-King model [4, 5], and the one-equation models of Baldwin-Barth [6] and Spalart-Allmaras [7] are tested and evaluated for accuracy and robustness by using them to simulate the unsteady flows passing an oscillating rigid NACA 0015 airfoil. Their conclusion is that the one-equation models provide significant improvement over the algebraic and half-equation models. The work of Bohbot et al.[8] provides a comparison between the Baldwin-Lomax solution and Spalart-Allmaras solution of the viscous flutter boundary prediction for a NACA64A010 airfoil. A significant difference can be observed between two predicted flutter boundaries from both turbulence models. Another example of 3-D aeroelastic computations for transonic flows has been given by Doi et al.[9]. They found that the $k-\omega$ model [10] was a suitable choice for prediction of flutter boundaries of turbomachinery components. Chen et al.[11, 12] have developed a fully coupled method for prediction of flutter boundaries of AGARD Wing 445.6 using the Baldwin-Lomax model. The Baldwin-Lomax model is found to be inadequate to predict complex flow field with massive unsteady separated zones [1] for aeroelastic simulations. Wang and zha successfully applied the DES to predict the LCO of NLR7301 airfoil [13] and [14] which use S-A model and predict the LCO as good as DES. An excellent quantitative agreement between the computation and experiement is achieved for both LCO frequency and amplitude. For a compressor rotor, the flow fields become more complicated since a flexible blade has many more degrees of freedom than a rigid body airfoil or a flexible wing. Therefore, the objective of this investigation is to apply the most recent turbulence closure method in the 3-D aeroelastic analysis.

Large eddy simulation (LES) is promising to overcome the disadvantages of the RANS model. In LES, the large energy containing scales are directly simulated, and the small scale eddies, which are generally more homogeneous and isotropic, are modeled. Because the statistics of the small scale turbulence are nearly homogeneous and isotropic, a general physical model for small scale eddies is more plausible. However, for high Reynolds number unsteady turbomachinery flows, LES is too expensive to resolve the wall boundary layer. As pointed by Spalart et al.[15], for engineering applications, it is not hopeful for LES to be rigorously used until in another 4 decades.

To bypass the expensive CPU requirement for LES in wall boundary layer computations, Spalart et al.[16] developed the so called detached eddy simulation (DES) strategy. DES is a hybrid method that transits the turbulence modeling from the RANS model near the wall to large eddy simulation (LES) in the region away from the wall. This approach is more generally applicable than RANS motheds in predicting complex unsteady flow with an affordable computational cost.

It is expected that the high fidelity DES will better predict the aerodynamic force acting on the rotor blades, which is crucial for FSI simulations. In present study, the resolved frequencies of the rotor blades are very high (5th mode shape frequency is about 6800 Hz) compared with the turbulence fluctuation frequency scale. Consequently, time-average RANS models will degrade the accuracy of numerical results.

Although DES is now powerful enough to solve practical engineering problems, it is still a challenging task to be accomplished in large scale complex geometries, such as rotor blades with tip clearance, especially if the fluid-structural interaction is of concern. Its LES part requires high-order numerical schemes to minimize the numerical diffusion so that the actual turbulent fluctuations will not be damped out. In addition to discretization schemes, the non-reflective boundary condition is also critical for accurate calculation of unsteady flows. This is particularly true for internal turbomachinery flows, in which the computational domain usually is confined near the solid objects. For example, previous study [17] indicates that different treatments of numerical perturbation at upstream and downstream boundaries can totally change the compressor blade stall inception pattern.

In present study, a DES fully coupled methodology for calculating flow-induced flexible body vibrations are used. The high accuracy numerical techniques include: a 5th order WENO scheme[18, 19] with a low diffusion E-CUSP scheme[20] for the inviscid fluxes, a fully conservative 4th order central differencing scheme[19] for the viscous terms, and a non-reflective boundary condition based on the concept of characteristic variables[21].

2 Numerical Approaches

2.1 Flow Governing Equations

To develop the simulation capability for turbomachinery applications, the Navier-Stokes equatins are transforred into a rotating frame about the x axis. By adding the Coriolis and centrifugal forces to the right hand side of the equations, the rotating flow problems can be treated as non-rotating ones. After the application of a spatially Favre-filtering process, the compressible Navier-Stokes equations can be transformed to the generalized coordinates and expressed as:

$$\frac{\partial \mathbf{Q}'}{\partial t} + \frac{\partial \mathbf{E}'}{\partial \xi} + \frac{\partial \mathbf{F}'}{\partial \eta} + \frac{\partial \mathbf{G}'}{\partial \zeta} = \frac{1}{Re}\left(\frac{\partial \mathbf{E_v}'}{\partial \xi} + \frac{\partial \mathbf{F_v}'}{\partial \eta} + \frac{\partial \mathbf{G_v}'}{\partial \zeta}\right) + \mathbf{S} \tag{1}$$

where Re is the Reynolds number and

$$\begin{gathered}
\mathbf{Q}' = \tfrac{\mathbf{Q}}{J} \\
\mathbf{E}' = \tfrac{1}{J}(\xi_t\mathbf{Q} + \xi_x\mathbf{E} + \xi_y\mathbf{F} + \xi_z\mathbf{G}),\ \mathbf{E_v}' = \tfrac{1}{J}(\xi_x\mathbf{E_v} + \xi_y\mathbf{F_v} + \xi_z\mathbf{G_v}) \\
\mathbf{F}' = \tfrac{1}{J}(\eta_t\mathbf{Q} + \eta_x\mathbf{E} + \eta_y\mathbf{F} + \eta_z\mathbf{G}),\ \mathbf{F_v}' = \tfrac{1}{J}(\eta_x\mathbf{E_v} + \eta_y\mathbf{F_v} + \eta_z\mathbf{G_v}) \\
\mathbf{G}' = \tfrac{1}{J}(\zeta_t\mathbf{Q} + \zeta_x\mathbf{E} + \zeta_y\mathbf{F} + \zeta_z\mathbf{G}),\ \mathbf{G_v}' = \tfrac{1}{J}(\zeta_x\mathbf{E_v} + \zeta_y\mathbf{F_v} + \zeta_z\mathbf{G_v})
\end{gathered}$$

where J is the transformation Jacobian. The variable vector $\mathbf{Q}$, and inviscid flux vectors $\mathbf{E}$, $\mathbf{F}$, and $\mathbf{G}$ are written as

$$\mathbf{Q} = \begin{bmatrix} \bar{\rho} \\ \bar{\rho}\tilde{u} \\ \bar{\rho}\tilde{v} \\ \bar{\rho}\tilde{w} \\ \bar{\rho}\tilde{e} \end{bmatrix}, \mathbf{E} = \begin{bmatrix} \bar{\rho}\tilde{u} \\ \bar{\rho}\tilde{u}\tilde{u} + \bar{p} \\ \bar{\rho}\tilde{u}\tilde{v} \\ \bar{\rho}\tilde{u}\tilde{w} \\ (\bar{\rho}\tilde{e} + \bar{p})\tilde{u} \end{bmatrix}, \mathbf{F} = \begin{bmatrix} \bar{\rho}\tilde{v} \\ \bar{\rho}\tilde{v}\tilde{u} \\ \bar{\rho}\tilde{v}\tilde{v} + \bar{p} \\ \bar{\rho}\tilde{v}\tilde{w} \\ (\bar{\rho}\tilde{e} + \bar{p})\tilde{v} \end{bmatrix}, \mathbf{G} = \begin{bmatrix} \bar{\rho}w \\ \bar{\rho}\tilde{w}\tilde{u} \\ \bar{\rho}\tilde{w}\tilde{v} \\ \bar{\rho}\tilde{w}\tilde{w} + \bar{p} \\ (\bar{\rho}\tilde{e} + \bar{p})\tilde{w} \end{bmatrix},$$

where ρ is the density, u, v, and w are the Cartesian velocity components in x, y and z directions, p is the static pressure, and e is the total energy per unit mass. The overbar denotes the spatial filtered quantity, tilde denotes the Favre-filtered quantity. All the flow variable in above equations are non-dimensionlized by using the freestream quantities and a reference length L. $\mathbf{E}'$, $\mathbf{F}'$, and $\mathbf{G}'$ are the inviscid fluxes at the moving grid system and can be expressed as

$$\mathbf{E}' = \begin{bmatrix} \bar{\rho}U \\ \bar{\rho}\tilde{u}U + l_x\bar{p} \\ \bar{\rho}\tilde{v}U + l_y\bar{p} \\ \bar{\rho}\tilde{w}U + l_z\bar{p} \\ (\bar{\rho}\tilde{e} + \bar{p})U - l_t\bar{p} \end{bmatrix}, \mathbf{F}' = \begin{bmatrix} \bar{\rho}V \\ \bar{\rho}\tilde{u}V + m_x\bar{p} \\ \bar{\rho}\tilde{v}V + m_y\bar{p} \\ \bar{\rho}\tilde{w}V + m_z\bar{p} \\ (\bar{\rho}\tilde{e} + \bar{p})V - m_t\bar{p} \end{bmatrix}, \mathbf{G}' = \begin{bmatrix} \bar{\rho}W \\ \bar{\rho}\tilde{u}W + n_x\bar{p} \\ \bar{\rho}\tilde{v}W + n_y\bar{p} \\ \bar{\rho}\tilde{w}W + n_z\bar{p} \\ (\bar{\rho}\tilde{e} + \bar{p})W - n_t\bar{p} \end{bmatrix},$$

where U, V and W are the contravariant velocities in ξ, η and ζ directions, and defined as

$$U = l_t + \mathbf{l} \bullet \mathbf{V} = l_t + l_x\tilde{u} + l_y\tilde{v} + l_z\tilde{w}$$

$$V = m_t + \mathbf{m} \bullet \mathbf{V} = m_t + m_x\tilde{u} + m_y\tilde{v} + m_z\tilde{w} \tag{2}$$

$$W = n_t + \mathbf{n} \bullet \mathbf{V} = n_t + n_x\tilde{u} + n_y\tilde{v} + n_z\tilde{w}$$

where l_t, m_t and n_t are the components of the interface contravariant velocity of the control volume in ξ, η and ζ directions respectively, $\mathbf{l}$, $\mathbf{m}$ and $\mathbf{n}$ are the normal vectors located at the centers of ξ, η and ζ interfaces of the control volume with their magnitudes equal to the surface areas and pointing to the directions of increasing ξ, η and ζ. These quantities are defined as

$$l_t = \frac{\xi_t}{J}, \quad m_t = \frac{\eta_t}{J}, \quad n_t = \frac{\zeta_t}{J}, \quad \mathbf{l} = \frac{\nabla\xi}{J}, \quad \mathbf{m} = \frac{\nabla\eta}{J}, \quad \mathbf{n} = \frac{\nabla\zeta}{J} \tag{3}$$

and the viscous flux vectors are given by

$$\mathbf{E_v} = \begin{bmatrix} 0 \\ \bar{\tau}_{xx} + \sigma_{xx} \\ \bar{\tau}_{xy} + \sigma_{xy} \\ \bar{\tau}_{xz} + \sigma_{xz} \\ Q_x \end{bmatrix}, \mathbf{F_v} = \begin{bmatrix} 0 \\ \bar{\tau}_{yx} + \sigma_{yx} \\ \bar{\tau}_{yy} + \sigma_{yy} \\ \bar{\tau}_{yz} + \sigma_{yz} \\ Q_y \end{bmatrix}, \mathbf{G_v} = \begin{bmatrix} 0 \\ \bar{\tau}_{zx} + \sigma_{zx} \\ \bar{\tau}_{zy} + \sigma_{zy} \\ \bar{\tau}_{zz} + \sigma_{zz} \\ Q_z \end{bmatrix}$$

Let subscript 1, 2 and 3 represent the coordinates, x, y, and z, and use Einstein summation convention, the shear-stress, the subgrid scale stress tensor, and Q_x, Q_y, Q_z terms in non-dimensional forms can be expressed in tensor form as

$$\bar{\tau}_{ij} = \frac{2}{3}\tilde{\mu}\frac{\partial \tilde{u}_k}{\partial x_k}\delta_{ij} + \tilde{\mu}(\frac{\partial \tilde{u}_i}{\partial x_j} + \frac{\partial \tilde{u}_j}{\partial x_i}) \tag{4}$$

$$\sigma_{ij} = -\bar{\rho}(\widetilde{u_i u_j} - \tilde{u}_i\tilde{u}_j) \tag{5}$$

$$Q_i = \tilde{u}_j(\bar{\tau}_{ij} + \sigma_{ij}) - \bar{q}_i + \Phi_i \tag{6}$$

In Eq.(4), the viscosity μ is the molecular viscosity and is determined by Sutherland law. Φ_i and $\bar{q}_i$ are the subscale heat flux and the mean molecular heat flux respectively, and take the forms:

$$\Phi_i = -C_p\bar{\rho}(\widetilde{u_i T} - \tilde{u}_i\tilde{T}) \tag{7}$$

$$\bar{q}_i = -\frac{C_p\tilde{\mu}}{Pr}\frac{\partial \tilde{T}}{\partial x_i} \tag{8}$$

where T is the temperature, C_p is the specific heat measured under constant pressure, and Pr is the Prandtl number. The equation of state closes the system as follow,

$$\bar{\rho}\tilde{e} = \frac{\tilde{p}}{(\gamma - 1)} + \frac{1}{2}\bar{\rho}(\tilde{u}^2 + \tilde{v}^2 + \tilde{w}^2) - \frac{1}{2}\bar{\rho}({v_\Omega}^2 + {w_\Omega}^2) + \bar{\rho}k \tag{9}$$

where γ is the ratio of specific heats, $v_\Omega = -\Omega z$ and $w_\Omega = \Omega y$ are the rotating velocity components, Ω is the rotating speed, $\bar{\rho}k$ is the subscale turbulence kinetic energy per unit volume and takes the form:

$$\bar{\rho}k = \frac{1}{2}\bar{\rho}(\widetilde{u_i u_i} - \tilde{u}_i\tilde{u}_i) \tag{10}$$

In the present study, the term $\bar{\rho}k$ is neglected based on the assumption that its effect is small. The source term S can be written as

$$\mathbf{S} = \begin{bmatrix} 0 \\ 0 \\ {R_o}^2 y\rho + 2R_o\rho w \\ {R_o}^2 z\rho - 2R_o\rho v \\ 0 \end{bmatrix} \tag{11}$$

where $R_o = \frac{\Omega L}{U}$ is the Rossby number, U and L are the reference velocity and length used in nondimensionalizing procedure.

2.2 Detached-Eddy Simulation

The DES suggested by Spalart et al.[15] is based on the Spalart-Allmaras one-equation turbulence model [7], which can be expressed in generalized coordinates as

$$\frac{\partial \frac{1}{J}\rho\tilde{\nu}}{\partial t} + \frac{\partial \rho\tilde{\nu}U}{\partial \xi} + \frac{\partial \rho\tilde{\nu}V}{\partial \eta} + \frac{\partial \rho\tilde{\nu}W}{\partial \zeta} = \frac{1}{Re}\left[\frac{\partial \frac{\rho}{\sigma}(\nu+\tilde{\nu})\mathbf{l}\bullet\nabla\tilde{\nu}}{\partial \xi} + \right.$$

$$\left. \frac{\partial \frac{\rho}{\sigma}(\nu+\tilde{\nu})\mathbf{m}\bullet\nabla\tilde{\nu}}{\partial \eta} + \frac{\partial \frac{\rho}{\sigma}(\nu+\tilde{\nu})\mathbf{n}\bullet\nabla\tilde{\nu}}{\partial \zeta} + \frac{1}{J}S_\nu\right] \tag{12}$$

where

$$S_\nu = \rho C_{b1}(1-f_{t2})\tilde{S}\tilde{\nu} + \frac{1}{Re}\left[-\rho\left(C_{w1}f_w - \frac{C_{b1}}{\kappa^2}f_{t2}\right)\left(\frac{\tilde{\nu}}{d}\right)^2 + \right.$$

$$\left. \frac{\rho}{\sigma}C_{b2}(\nabla\tilde{\nu})^2 - \frac{1}{\sigma}\left(\nu+\tilde{\nu}\right)\nabla\tilde{\nu}\bullet\nabla\rho\right] + Re\left[\rho f_{t1}(\triangle)^2\right] \tag{13}$$

The turbulent eddy viscosity is calculated from

$$\nu_t = \tilde{\nu}f_{v1}, \qquad f_{v1} = \frac{\chi^3}{\chi^3 + c_{v1}^3}, \qquad \chi = \frac{\tilde{\nu}}{\nu} \tag{14}$$

where ν is the molecular viscosity. The production term is expressed as

$$\tilde{S} = S + \frac{\tilde{\nu}}{k^2 d^2}f_{v2}, \qquad\qquad f_{v2} = 1 - \frac{\chi}{1+\chi f_{v1}}$$

where S is the magnitude of the vorticity. The DES is formulated by replacing the distance to the nearest wall, d, in the Spalart-Allmaras model with a modified distance

$$\tilde{d} = min(d, C_{DES}\Delta) \tag{15}$$

where Δ is the largest spacing of the grid cell and C_{DES} is a constant. This mechanism enables DES to behave as a RANS model in the near-wall regions, and the LES away from the walls. Consequently, the subgrid scale stress tensor can be modeled in the following way:

$$\sigma_{ij} = \mu_{DES} \left(\frac{\partial \tilde{u}_i}{\partial x_j} + \frac{\partial \tilde{u}_j}{\partial x_i} - \frac{2}{3} \frac{\partial \tilde{u}_k}{\partial x_k} \delta_{ij} \right) \tag{16}$$

where

$$\mu_{DES} = \bar{\rho} \nu_t = \bar{\rho} \tilde{\nu} f_{v1} \tag{17}$$

The subscale heat flux can calculated using the following equation:

$$\Phi_i = \frac{C_p \mu_{DES}}{Pr_t} \frac{\partial \tilde{T}}{\partial x_i} \tag{18}$$

where Pr_t is the turbulent Prandtl number. More details of the Spalart DES model can be found in[15, 22, 13].

2.3 The Low Diffusion E-CUSP (LDE) Scheme[20]

In generalized coordinate system, the flux **E** can be split as the following:

$$\mathbf{E}' = E^c + E^p = \begin{pmatrix} \rho U \\ \rho u U \\ \rho v U \\ \rho w U \\ \rho e U \\ \rho \tilde{\nu} U \end{pmatrix} + \begin{pmatrix} 0 \\ l_x p \\ l_y p \\ l_z p \\ p \overline{U} \\ 0 \end{pmatrix} \tag{19}$$

where, U is the contravariant velocity in ξ direction and is defined as the following:

$$U = l_t + l_x u + l_y v + l_z w \tag{20}$$

$\overline{U}$ is defined as:

$$\overline{U} = l_x u + l_y v + l_z w \tag{21}$$

The convective term, E^c is evaluated by

$$E^c = \rho U \begin{pmatrix} 1 \\ u \\ v \\ w \\ e \\ \tilde{\nu} \end{pmatrix} = \rho U f^c, \ f^c = \begin{pmatrix} 1 \\ u \\ v \\ w \\ e \\ \tilde{\nu} \end{pmatrix} \tag{22}$$

let

$$C = c \left(l_x^2 + l_y^2 + l_z^2 \right)^{\frac{1}{2}} \tag{23}$$

where $c = \sqrt{\gamma R T}$ is the speed of sound. Then the convective flux at interface $i + \frac{1}{2}$ is evaluated as:

$$E^c_{i+\frac{1}{2}} = C_{\frac{1}{2}} \left[\rho_L C^+ f^c_L + \rho_R C^- f^c_R\right] \tag{24}$$

where, the subscripts L and R represent the left and right hand sides of the interface. The Mach number splitting of Edwards[23, 24] is borrowed to determine c^+ and c^- as the following:

$$\begin{aligned}
&C_{\frac{1}{2}} = \tfrac{1}{2}\left(C_L + C_R\right),\ C^+ = \alpha^+_L\left(1+\beta_L\right)M_L - \beta_L M^+_L - M^+_{\frac{1}{2}}\\
&C^- = \alpha^-_R\left(1+\beta_R\right)M_R - \beta_R M^-_R + M^-_{\frac{1}{2}}\\
&M_L = \tfrac{U_L}{C_{\frac{1}{2}}},\ M_R = \tfrac{U_R}{C_{\frac{1}{2}}}\\
&\alpha_{L,R} = \tfrac{1}{2}\left[1 \pm sign\left(M_{L,R}\right)\right]\\
&\beta_{L,R} = -max\left[0, 1 - int\left(|M_{L,R}|\right)\right]\\
&M^+_{\frac{1}{2}} = M_{\frac{1}{2}}\tfrac{C_R + C_L\Phi}{C_R + C_L},\ M^-_{\frac{1}{2}} = M_{\frac{1}{2}}\tfrac{C_L + C_R\Phi^{-1}}{C_R + C_L},\ \Phi = \tfrac{\left(\rho C^2\right)_R}{\left(\rho C^2\right)_L}\\
&M_{\frac{1}{2}} = \beta_L\delta^+ M^-_L - \beta_R\delta^- M^+_R\\
&M^{\pm}_{L,R} = \pm\tfrac{1}{4}\left(M_{L,R} \pm 1\right)^2\\
&\delta^{\pm} = \tfrac{1}{2}\left\{1 \pm sign\left[\tfrac{1}{2}\left(M_L + M_R\right)\right]\right\}
\end{aligned}$$

The pressure flux, E^p is evaluated as the following

$$E^p_{i+\frac{1}{2}} = \begin{pmatrix} 0 \\ \mathcal{P}^+ p\, l_x \\ \mathcal{P}^+ p\, l_y \\ \mathcal{P}^+ p\, l_z \\ \frac{1}{2}p\left[\overline{U} + \overline{C}_{\frac{1}{2}}\right] \\ 0 \end{pmatrix}_L + \begin{pmatrix} 0 \\ \mathcal{P}^- p\, l_x \\ \mathcal{P}^- p\, l_y \\ \mathcal{P}^- p\, l_z \\ \frac{1}{2}p\left[\overline{U} - \overline{C}_{\frac{1}{2}}\right] \\ 0 \end{pmatrix}_R \tag{25}$$

The contravariant speed of sound $\overline{C}$ in the pressure vector is consistent with $\overline{U}$. It is computed based on C as the following,

$$\overline{C} = C - l_t \tag{26}$$

The use of $\overline{U}$ and $\overline{C}$ instead of U and C in the pressure vector is to take into account of the grid speed so that the flux will transit from subsonic to supersonic smoothly. When the grid is stationary, $l_t = 0$, $\overline{C} = C$, $\overline{U} = U$.

The LDE scheme can capture crisp shock profile and exact contact surface discontinuities as accurately as the Roe scheme[20]. However, it is simpler and more CPU efficient than the Roe scheme due to no matrix operation.

2.4 Time Marching Scheme

The unsteady compressible Navier-Stokes equations (1) coupled to the Spalart-Allmaras turbulence equation (12) are solved using the control volume method with the concept of dual time stepping suggested by Jameson[25]. A pseudo temporal term $\frac{\partial \mathbf{Q}}{\partial \tau}$ is added to the governing equation (1). This term vanishes at the end of each physical time step, and has no influence on the accuracy of the solution. However, instead of using the explicit scheme as in [25], an implicit pseudo time marching scheme using line Gauss-Seidel iteration is employed to achieve high convergence rate. For unsteady time accurate computations, the temporal term is discretized implicitly using a three point, backward differencing as the following

$$\frac{\partial \mathbf{Q}}{\partial t} = \frac{3Q^{n+1} - 4Q^n + Q^{n-1}}{2\Delta t} \tag{27}$$

Where n is the time level index. The pseudo temporal term is discretized with first order Euler scheme. Let m stand for the iteration index within a physical time step, the semi-discretized governing equation (1) can be expressed as

$$[(\frac{1}{\Delta\tau} + \frac{1.5}{\Delta t})I - (\frac{\partial R}{\partial Q})^{n+1,m}]\delta Q^{n+1,m+1} = R^{n+1,m} - \frac{3Q^{n+1,m} - 4Q^n + Q^{n-1}}{2\Delta t} \tag{28}$$

where the $\Delta\tau$ is the pseudo time step, R is the net flux evaluated at a grid point. Equation (28) is solved using the unfactored line Gauss-Seidel iteration.

2.5 Boundary Conditions

The boundary conditions for the computation of wing flutter are as follows:

(1) Upstream boundary conditions[26]: Total pressure P_{total}, total temperature T_{total}, and flow angles α_1, α_2 are given at subsonic inlet. The speed of sound at the boundary can be calculated as

$$c_b = \frac{-B + \sqrt{B^2 - 4AC}}{2A} \tag{29}$$

where

$$A = cos\theta^2 + \frac{2}{\gamma - 1}, \qquad B = 2J^-, \qquad C = \frac{\gamma - 1}{2}J^{-2} - T^* cos\theta^2 \tag{30}$$

$$J^- = u_i - \frac{2c_i}{\gamma - 1}, \qquad T^* = {c_i}^2 + (\gamma - 1)\frac{1}{2}({u_i}^2 + {v_i}^2 + {w_i}^2) \tag{31}$$

$$t_o = T_{total}\frac{{c_i}^2}{T^*}, \qquad p_o = P_{total}(\frac{t_o}{T_{total}})^{\frac{\gamma}{\gamma-1}}, \qquad \rho_o = \gamma\frac{p_o}{{c_b}^2}, \tag{32}$$

$$u_o = \frac{1}{M_\infty}\sqrt{\frac{T_{total} - t_o}{\frac{1}{2}(\gamma - 1)(1 + {k_1}^2 + {k_2}^2)}}, \qquad v_o = u_o tan(\alpha_1), \qquad w_o = u_o tan(\alpha_2) \tag{33}$$

$$(\rho u)_o = \rho_o u_o, \qquad (\rho v)_o = \rho_o v_o, \qquad (\rho w)_o = \rho_o w_o \tag{34}$$

$$(\rho e)_o = \frac{p_o}{\gamma - 1} + \rho_o[\frac{1}{2}({u_o}^2 + {v_o}^2 + {w_o}^2) - \frac{1}{2}({v_\Omega}^2 + {w_\Omega}^2)] \tag{35}$$

where the subscripts i and o represent the values at the $1st$ interior cell close to the boundary and at phantom cell respectively.

(2) Downstream boundary conditions: A non-reflective boundary condition has been implemented at the outlet of the rotor based on the concept of characteristic variables as described in[21]. The outlet pressure p_{outlet} is given to achieve an unique mass flow rate through the rotor. The pressure at phantom cell is given by

$$p_o = p_i - \bar{p} + p_{outlet} \tag{36}$$

where

$$\bar{p} = \frac{1}{A}\int_A p_i dA \tag{37}$$

and A is the cross-sectional area of the outlet. Other variables can be calculated by

$$\rho_o = \rho_i + \frac{p_o - p_i}{{c_i}^2}, \qquad u_o = u_i - n_x \frac{p_o - p_i}{\rho_i c_i}, \qquad v_o = v_i - n_y \frac{p_o - p_i}{\rho_i c_i}, \qquad w_o = w_i - n_z \frac{p_o - p_i}{\rho_i c_i} \tag{38}$$

where n_x, n_y and n_z are the unit normal vector points out of the domain.

$$(\rho u)_o = \rho_o u_o, \qquad (\rho v)_o = \rho_o v_o, \qquad (\rho w)_o = \rho_o w_o \tag{39}$$

$$(\rho e)_o = \frac{p_o}{\gamma - 1} + \rho_o[\frac{1}{2}({u_o}^2 + {v_o}^2 + {w_o}^2) - \frac{1}{2}({v_\Omega}^2 + {w_\Omega}^2)] \tag{40}$$

(3) Solid wall boundary conditions: At moving boundary surface, the no-slip condition is enforced by extrapolating the velocity between the phantom and interior cells,

$$u_0 = 2\dot{x}_b - u_1, \qquad v_0 = 2\dot{y}_b - v_1, \qquad w_0 = 2\dot{z}_b - w_1 \tag{41}$$

where u_0, v_0 and w_0 denote the velocity at phantom cell, u_1, v_1 and w_1 denote the velocity at the $1st$ interior cell close to the boundary, and u_b, v_b and w_b are the velocity on the moving boundary.

If the wall surface is in η direction, the other two conditions to be imposed on the solid wall are the adiabatic wall condition and the inviscid normal momentum equation[27] as follows,

$$\frac{\partial T}{\partial \eta} = 0, \qquad \frac{\partial p}{\partial \eta} = -\left(\frac{\rho}{\eta_x^2 + \eta_y^2 + \eta_z^2}\right)(\eta_x \ddot{x}_b + \eta_y \ddot{y}_b + \eta_z \ddot{z}_b) \tag{42}$$

3 Modal Approach of Three Dimensional Rotor Blade

The calculation based on fully coupled iteration is CPU expensive, especially for three dimensional applications. The modal approach can save CPU time significantly by solving modal displacement equations, Equation (52), instead of the original structural equations, Equation (45), which is usually solved by using finite element method. In the modal approach, the structural mode shapes can be pre-determined by using a separate finite element structural solver. Once the several mode shapes of interest are obtained, the physical displacements can be calculated just by solving those simplified linear equations, Equation (52) and Equation (46). In present study, the first five mode shapes provided in Ref.[28] are used to model the wing structure. These pre-calculated mode shapes are obtained on a structural grid system and are transformed to the CFD grid system by using a 3rd order polynomial fitting procedure. The procedure is only performed once and then the mode shapes for CFD grid system are stored in the code throughout the simulation. To validate the structural model used in the present study, the dynamic responses of a flexible plate wing is calculated and compared with the results by using the finite element solver ANSYS. The plate wing has the same outline as the AGARD wing 445.6, and its first mode natural vibration frequency is nearly the same as the corresponding one of the AGARD wing 445.6. The numerical predictions by the present structural solver with first five mode shapes agree excellently with the results using ANSYS with first five mode shapes and the full structural model [12].

The governing equation of the solid structure motion can be written as,

$$\mathbf{M}\frac{d^2\mathbf{u}}{dt^2} + \mathbf{C}\frac{d\mathbf{u}}{dt} + \mathbf{K}\mathbf{u} = \mathbf{f} \tag{43}$$

where $\mathbf{M}$, $\mathbf{C}$ and $\mathbf{K}$ are the mass, damping, and stiffness matrices of the solid respectively, $\mathbf{u}$ is the displacement vector and $\mathbf{f}$ is the force exerted on the surface node points of the solid, both can be expressed as:

$$\mathbf{u} = \begin{pmatrix} \mathbf{u}_1 \\ \vdots \\ \mathbf{u}_i \\ \vdots \\ \mathbf{u}_N \end{pmatrix}, \mathbf{f} = \begin{pmatrix} \mathbf{f}_1 \\ \vdots \\ \mathbf{f}_i \\ \vdots \\ \mathbf{f}_N \end{pmatrix},$$

where N is the total number of node points of the structural model, $\mathbf{u}_i$ and $\mathbf{f}_i$ are vecters with 3 components in x, y, z directions:

$$\mathbf{u}_i = \begin{pmatrix} \mathbf{u}_{ix} \\ \mathbf{u}_{iy} \\ \mathbf{u}_{iz} \end{pmatrix}, \mathbf{f}_i = \begin{pmatrix} \mathbf{f}_{ix} \\ \mathbf{f}_{iy} \\ \mathbf{f}_{iz} \end{pmatrix}.$$

$\mathbf{f}_i$ is dynamic force exerted on the surface of the solid body. In a modal approach, the modal decomposition of the structure motion can be expressed as follows:

$$\mathbf{K\Phi} = \mathbf{M\Phi\Lambda} \tag{44}$$

or

$$\mathbf{K}\phi_j = \lambda_j\mathbf{M}\phi_j \tag{45}$$

where $\mathbf{\Lambda}$ is eigenvalue matrix, $\mathbf{\Lambda} = diag[\lambda_1, \cdots, \lambda_j, \cdots, \lambda_{3N}]$, and jth eigenvalue $\lambda_j = {\omega_j}^2$, ω_j is the natural frequency of jth mode, and the mode shape matrix $\mathbf{\Phi} = [\phi_1, \cdots, \phi_j, \cdots, \phi_{3N}]$.

Equation (45) can be solved by using a finite element solver (e.g. ANSYS) to obtain its finite number of mode shapes ϕ_j. The first five mode shapes will be used in this paper to calculate the displacement of the structure such that,

$$\mathbf{u}(t) = \sum_j a_j(t)\phi_j = \mathbf{\Phi a} \tag{46}$$

where $\mathbf{a} = [a_1, a_2, a_3, a_4, a_5]^T$. Substitute Equation (46) to Equation (43) and yield

$$\mathbf{M\Phi}\frac{d^2\mathbf{a}}{dt^2} + \mathbf{C\Phi}\frac{d\mathbf{a}}{dt} + \mathbf{K\Phi a} = \mathbf{f} \tag{47}$$

Multiply Equation (47) by $\mathbf{\Phi}^T$ and re-write it as

$$\hat{\mathbf{M}}\frac{d^2\mathbf{a}}{dt^2} + \hat{\mathbf{C}}\frac{d\mathbf{a}}{dt} + \hat{\mathbf{K}}\mathbf{a} = \mathbf{P} \tag{48}$$

where $\mathbf{P} = [P_1, P_2, \cdots, P_j, \cdots, P_N]^T$, the modal force of jth mode, $P_j = \phi_j^T\mathbf{f}$, the modal mass matrix is defined as

$$\hat{\mathbf{M}} = \mathbf{\Phi}^T\mathbf{M}\mathbf{\Phi} = diag(m_1, \cdots, m_j, \cdots, m_{3N}) \tag{49}$$

where m_j is the modal mass of jth mode, and the modal damping matrix is defined as

$$\hat{\mathbf{C}} = \mathbf{\Phi}^T\mathbf{C}\mathbf{\Phi} = diag(c_1, \cdots, c_j, \cdots, c_{3N}) \tag{50}$$

where c_j is the modal damping of jth mode, and the modal stiffness matrix is defined as

$$\hat{\mathbf{K}} = \mathbf{\Phi}^T\mathbf{K}\mathbf{\Phi} = diag(k_1, \cdots, k_j, \cdots, k_{3N}) \tag{51}$$

where k_j is the modal stiffness of jth mode. Equation (48) implies

$$\frac{d^2a_j}{dt^2} + 2\zeta_j\omega_j\frac{da_j}{dt} + \omega_j^2a_j = \frac{\phi_j^T\mathbf{f}}{m_j} \tag{52}$$

where ζ_j is modal damping ratio. Equation (52) is the modal equation of structure motion, and is solved numerically within each iteration. By carefully choosing reference quantities, the normalized equation may be expressed as

$$\frac{d^2a_j}{dt^{*2}} + 2\zeta_j\left(\frac{\omega_j}{\omega_\alpha}\right)\frac{da_j}{dt^*} + \left(\frac{\omega_j}{\omega_\alpha}\right)^2 a_j = \phi_j^{*T}\mathbf{f}^*V^*\left(\frac{b_s}{L}\right)^2\frac{\bar{m}}{v^*} \tag{53}$$

where the dimensionless quantities are denoted by an asterisk, ω_α is the natural frequency in pitch, b_s is the streamwise semichord measured at wing root, L is the reference length, $\bar{m}$ is the measured wing panel mass, v^* is the volume of a conical frustum having streamwise root chord as lower base diameter, streamwise tip chord as upper base diameter, and panel span as height, $V^* = \frac{U_\infty}{b_s\omega_\alpha\sqrt{\bar{\mu}}}$, and U_∞ is the freestream velocity.

Then the equations are transformed to a state form and expressed as:

$$[\mathbf{M}]\frac{\partial\{\mathbf{S}\}}{\partial t} + [\mathbf{K}]\{\mathbf{S}\} = \mathbf{q} \tag{54}$$

where

$$\mathbf{S} = \begin{pmatrix} a_j \\ \dot{a}_j \end{pmatrix}, \mathbf{M} = [I], \mathbf{K} = \begin{pmatrix} 0 & -1 \\ \left(\frac{\omega_j}{\omega_\alpha}\right)^2 & 2\zeta\left(\frac{\omega_j}{\omega_\alpha}\right) \end{pmatrix}, \mathbf{q} = \begin{pmatrix} 0 \\ \phi_j^{*T}\mathbf{f}^*V^*\left(\frac{b_s}{L}\right)^2\frac{\bar{m}}{v^*} \end{pmatrix}.$$

To couple the structural equations with the equations of flow motion and solve them implicitly in each physical time step, above equations are discretized and integrated in a manner consistent with Equation (28) to yield

$$\left(\frac{1}{\Delta\tau}\mathbf{I} + \frac{1.5}{\Delta t}\mathbf{M} + \mathbf{K}\right)\delta S^{n+1,m+1} = -\mathbf{M}\frac{3\mathbf{S}^{n+1,m} - 4\mathbf{S}^n + \mathbf{S}^{n-1}}{2\Delta t} - \mathbf{K}\mathbf{S}^{n+1,m} + \mathbf{q}^{n+1,m+1} \tag{55}$$

where n is the physical time level index while m stands for the pseudo time index. The detailed coupling procedure between the fluid and structural systems is given in the following section.

4 Fully Coupled FSI Procedure

In the fully-coupled computation, the remeshing is performed in each iteration. Therefore, a CPU time efficient algebraic grid deformation method is employed in the computation instead of the commonly-used grid generation method in which the Poisson equation is solved for grid points. It is shown that the method can maintain the initial grid quality and keep almost the same mesh distribution around the solid body surface. The details on the implementation can be found in Ref.[12].

In order to reduce or avoid the error caused by the mixed temporal and spatial derivatives after a discretization procedure, the geometric conservation law suggested by Thomas et al.[29] needs to be enforced. To implement this option in the flow solver, the following term should be added to the right-hand side of Eq.(1):

$$\mathbf{S} = \mathbf{Q}\left[\frac{\partial J^{-1}}{\partial t} + \left(\frac{\xi_t}{J}\right)_\xi + \left(\frac{\eta_t}{J}\right)_\eta + \left(\frac{\zeta_t}{J}\right)_\zeta\right] \tag{56}$$

To rigorously simulate fluid-structural interactions, the equations of flow motion and structural response need to be solved simultaneously within each iteration in a fully coupled numerical model. The procedure of the fully coupled fluid-structure interaction can be seen in the flow chart given in Figure 1.

The code is developed as a multiblock flow solver for massively paralle computers. A general subdomain bounadry mapping procedure is applied [30]. Both fluid and structural information on the hallo cells is exachanged asynchronously after each iteration. In other words, the send and receive calls return immediatly when the message is still processed. The communication between blocks is operated by MPI.

5 Results and Discussion

The NASA Lewis research transonic compressor Rotor 37 is used as test case to validate the 3-D CFD solver. The rotor was designed and tested by Reid and Moore[31, 32], and was re-tested as a single-stage compressor and the corresponding experimental data were reported in[33, 34]. The steady state result is calculated first, and then used as initial flow field field for the unsteady FSI simulation.

5.1 Steady State Solutions of NASA Rotor 37

As a validation of the CFD solver for a 3-D compressor, the steady state solution of the transonic NASA Rotor 37 is calculated. It has 36 blades, a design rotating speed of 17189 (rpm), and a design pressure ratio of 2.106 at a mass flow rate of 20.19 (kg/sec). The freestream conditions for this study are listed in Table 1 below.

A multiblock grid system for single blade passage computation is generated and shown in Fig.2. There are 10 blocks placed around the blade, and 2 blocks generated to fill the hole in the tip clearance region above the blade. Each block around the blade consists of 17×37×48 grid points, whereas each block above the blade consists of 81×10×8 grid points. Each block overlaps its neighbors by a number of grid layers which are needed for a prescribed accuracy of the spatial descretization. The surface mesh of the blade and the hub is depicted in Fig.3. Fig.4 shows the computed relative Mach number contours on three different ζ cross-sections, and how the shock waves migrate along the radial direction at near-peak

Table 1: Free-stream condition for NASA Rotor 37

Mach number	0.6125
total pressure (psi)	14.7
total temperature (R)	519.0
p_{exit}/total pressure	1.225
Reynolds Number	1.2×10^6

efficiency condition. Figs.5, 6 and 7 compare computed radial profiles of adiabatic efficiency, total pressure, and total temperature at the exit of the rotor with experimental data at 98% of the maximum mass flow rate. As shown in the figures, the computed performance parameters agree well with the experimental data[35].

5.2 Stall Flutter

The single blade structure is modeled by its first five natural vibration mode shapes generated by using commercial solver ABAQUS. The design rotating speed is 17188.7 *rpm*. The blade is made of Maraging 200 with a density of 8200 kg/m^3 approximately. Accordingly, the estimated flutter speed index (FSI), V^*, is about 0.03593. To capture the possible flutters, the computations were performed along the entire design speed line. The overall performance is shown in Figs. 8 and 9.

The simulations start with the stationary rigid body blade model. After the unsteady state flow field around the blade is fully developed, the rigid body wing is switched to the flexible blade model. As a small imposed perturbation, the first mode displacement of the blade structural motion is set into sinusoidal motion for one cycle with the maximum amplitude of 0.0001 and the first mode frequency of the blade. Then the blade is allowed to deflect in response to the dynamic force load. Within each physical time step, the solution is usually converged with 20-30 iterations.

The time histories of generalized displacements of the rotor blade are plotted for three operating conditions, namely C, D, F in Fig.10 through Fig.15. Fig.10 and Fig.13 show damped responses of fisrt five modes at condition C. This condition is still away from the stall point. The flow unsteadiness is not strong enough to trigger the flutter. The amplitudes of all modes decrease with time. Condition D is the critical point. The initiations of flutter can be observed in Fig.11 and Fig.14. At condition F, the diverging responses of all five modes are obtained as shown in Fig.12 and Fig.15.

Fig.16 shows time histories of mass flows. A frequency analysis shows that all the frequencies of three mass flows are identical to the one of first mode oscillation. Consequently, the mass flows oscillation is generated due the movement of the first mode of the blade. From Fig.16, it can been seen that the oscillation amplitude of the mass flows is smaller when the operating condition is away from the stall point. When the operating condition approaches the stall point, the oscillation amplitude of the mass flows increases and the averaged mass flow decreases due to the stalled flow blockage. It implies that the flow unsteadiness is getting stronger when the opereting condition approaches to the stall point.

A comparison has been made between a flexible blade and a rigid blade. The time histories of mass flows are plotted in Fig.17 at condition F. For flexible blade model, the stall starts and the mass flow decreases dramatically around dimensionless time equal to 40 while there is no evidence for the occurrence of stalll if rigid blade model is used. It means that the fluid and blade interaction could initiate stall early.

6 Conclusion

A high fidelity detached eddy simulation (DES) of 3-D fluid-structural interaction is presented for predicting blade flutters in a transonic compressor rotor at near stall conditions. The numerical techniques used in the study include: implicit unfactored Gauss-Seidel iteration, 5th order WENO scheme with a low diffusion Riemann solver for the inviscid fluxes, a fully conservative 4th order central differencing scheme for the viscous terms, the Spalart one-equation DES model to transit the turbulence modeling from the RANS model near the wall to large eddy simulation (LES) in the region away from the wall, a non-reflective boundary conditions based on the concept of characteristic variables, and a fully coupled fluid-structural interaction methodology.

An efficient and accurate modal approach solver is used for simulating the structural responses with first five major mode shapes of the blade. The solver is developed as a massively parallel multiblock code using an efficient general sub-domain boundary mapping procedure, and has shown to have excellent scaling properties.

The steady performance parameters computed on a single blade passage domain compare favorably with experimental data for NASA rotor 37. For the FSI simulation with a single blade passage domain, the basic dynamic aeroelastic characteristics, such as damped and diverging blade responses have been captured successfully.

The simulation indicates that the rotor mass flow oscillates with the first mode of blade vibration. At stall flutter condition, the vibrating blade induces the rotor stall, whereas the rigid blade does not.

7 Acknowledgement

This research is supported by the funding of Air Force Research Lab under GUIde Consortium grant 09-GUIDE-1010.

References

[1] G. Srinivasan, J. Ekaterinaris, and W. McCroskey, "Evaluation of Turbulence Models for Unsteady Flows of an Oscillating Airfoil," *Journal of Computers and Fluids*, vol. 24, pp. 833–861, 1995.

[2] B. Baldwin and H. Lomax, "Thin-Layer Approximation and Algebraic Model for Separated Turbulent flows." AIAA Paper 78-257, 1978.

[3] V. Yakhot and S. Orzag, "Renormalization group analysis of turbulence. I. Basic theory," *Journal of Scientific Computing*, vol. 1, pp. 3–51, 1986.

[4] D. Johnson and L. King, "A mathematically simple turbulence closure model for attached and separated turbulent boundary layers," *AIAA Journal*, vol. 23, p. 1684, 1985.

[5] D. Johnson, "Nonequilibrium algebraic turbulence modeling considerations for transonic airfoil and wings," 1992.

[6] B. Baldwin and A. Barth, "A one-equation turbulence transport model for high reynolds number wall-bounded flows." AIAA Paper 91-0610, 1991.

[7] P. Spalart and S. Allmaras, "A one-equation turbulence model for aerodynamic flows." AIAA Paper 92-0439, 1992.

[8] J. Bohbot, J. Garnier, S. Toumit, and D. Darracq, "Computation of the Flutter Boundary of an Airfoil with a Parallel Navier-Stokes Solver." AIAA Paper 2001-0572, 2001.

[9] H. Doi and J. Alonso, "Fluid/Structure Coupled Aeroelastic Computations for Transonic Flows in Turbomachinery." ASME Turbo Expo 2002, GT-2002-30313, 2002.

[10] J. Yao, A. Jameson, J. Alonso, and F. Liu, "Development and Validation of a Massively Parallel Flow Solver for Turbomachinery Flows." AIAA Paper 00-0882, 2000.

[11] X.-Y. Chen, G.-C. Zha, and M.-T. Yang, "3D Simulation of a Transonic Wing Flutter using an Efficient High Resolution Upwind Scheme." AIAA Paper 2006-3216, 2006.

[12] X.-Y. Chen, G.-C. Zha, and M.-T. Yang, "Numerical Simulation of 3-D Wing Flutter with Fully Coupled Fluid-Structural Interaction," *Journal of Computers and Fluids*, vol. 35, pp. 856–867, 2007.

[13] B.-Y. Wang and G.-C. Zha, "Detached-Eddy Simulation of Transonic Airfoil Limited Cycle Oscillation with High Order WENO Scheme." AIAA Paper 2009-1507, 2008.

[14] B.-Y. Wang and G.-C. Zha, "Numerical simulation of transonic limit cycle oscillations using high-order low-diffusion schemes," *Journal of Fluids and Structures*, vol. doi:10.1016, p. j.jfluidstructs.2010.02.003, 2010.

[15] P. Spalart, W. Jou, M. Streletes, and S. Allmaras, "Comments on the Feasibility of LES for Wings and a Hybrid RANS/LES Approach." First AFSOR International Conference on DNS/LES, 1997.

[16] P. R. Spalart, "Young-Person's Guide to Detached-Eddy Simulation Grids." NASA/CR-2001-211032, 2001.

[17] L. He, "Computational Study of Rotating Stall Inception in Axial Compressors," *Journal of Propulsion and Power*, vol. 13, pp. 31–38, 1997.

[18] C.-W. Shu, "Essentially Non-Oscillatory and Weighted Essentially Schemesfor Hyperbolic Conservation Laws." NASA/CR-97-206253, 1997.

[19] Y.-Q. Shen, B.-Y. Wang, and G.-C. Zha, "Implicit WENO Scheme and High Order Viscous Formulas for Compressible Flows ." AIAA Paper 2007-4431, 2007.

[20] G.-C. Zha, Y. Shen, and B. Wang, "Calculation of Transonic Flows Using WENO Method with a Low Diffusion E-CUSP Upwind Scheme." AIAA Paper 2008-0745, 46th AIAA Aerospace Sciences Meeting, Reno, NV, Jan. 2008.

[21] D. Whitfield and J. Janus, "Three-Dimensional Unsteady Euler Equations Solution Using Flux Vector Splitting." AIAA Paper 1984-1552, 1984.

[22] B. Wang, G. Zha, and Y. Shen, "Detached-Eddy Simulations of a Circular Cylinder Using a Low Diffusion E-CUSP and High-Order WENO Scheme." AIAA Paper 2008-3855, 2008.

[23] J. R. Edwards, "A Low-Diffusion Flux-Splitting Scheme for Navier-Stokes Calculations." AIAA Paper 95-1703-CP, June, 1995.

[24] J. R. Edwards, "A Low-Diffusion Flux-Splitting Scheme for Navier-Stokes Calculations," *Computer & Fluids*, vol. 6, pp. 635–659, 1997.

[25] A. Jameson, "Time Dependent Calculations Using Multigrid with Application to Unsteady Flows past Airfoils and Wings." AIAA Paper 91-1596, 1991.

[26] F.-F. Ning and L.-P. Xu, “Numerical Simulation of Internal Flow in a Transonic Compressor with Complex Geometries.” Ph.D. Thesis, Beijing University of Aeronautics and Astronautics, February 2002.

[27] S. A. Morton, R. B. Melville, and M. R. Visbal, “Accuracy and Coupling Issues of Aeroelastic Navier-Stokes Solutions on Deforming Meshes.” AIAA Paper-97-1085, 1997.

[28] E. Yates Jr., “Agard standard aeroelastic configurations for dynamic response i.-wing 445.6,” Tech. Rep. AGARD Report No.765, AGARD, September 1985.

[29] P. Thomas and C. Lombard, “Geometric Conservation Law and Its Application to Flow Computations on Moving Grids,” *AIAA Journal*, vol. 17, pp. 1030–1037, 1979.

[30] B. Wang and G.-C. Zha, “A General Sub-Domain Boundary Mapping Procedure for Structured Grid CFD Parallel Computation.” AIAA Paper 2007-4432, 2007.

[31] L. Reid and R. Moore, “Design and Overall Performance of Four Highly-Loaded, High-Speed Inlet Stages for an Advanced, High-Pressure-Ratio Core Compressor.” NASA TP-1337, 1978.

[32] L. Reid and R. Moore, “Experimental Study of Low Aspect Ratio Compressor Blading.” ASME Paper 80-GT-6, 1980.

[33] K. Suder and A. Strazisar, “CFD Code Assessment in Turbomachinery-Data Report.” ASME Turbomachinery Committee, 1994.

[34] A. Strazisar and J. Denton, “CFD code assessment in turbomachinery - a progress report.” IGTI Global Gas Turbine News, 1995.

[35] J. Dunham, “Cfd validation for propulsion system components,” Tech. Rep. AGARD Report AR-355, AGARD, May 1998.

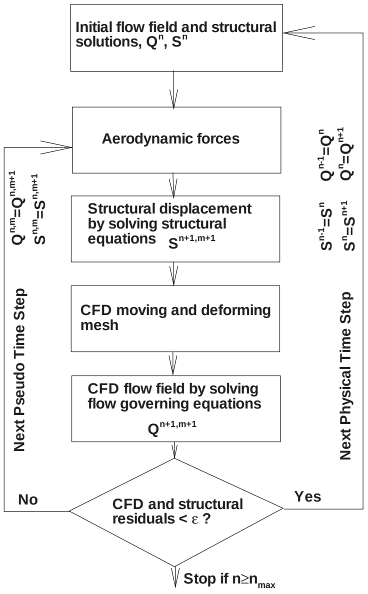

Figure 1: Fully coupled flow-structure interaction procedure.

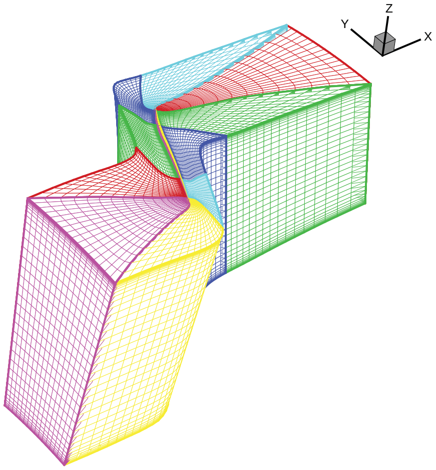

Figure 2: Multiblock grid system for single blade passage.

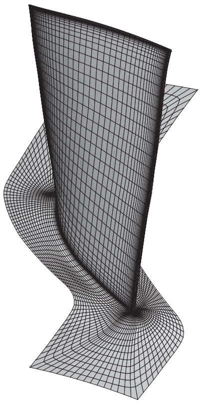

Figure 3: Mesh on the solid surfaces of blade and hub.

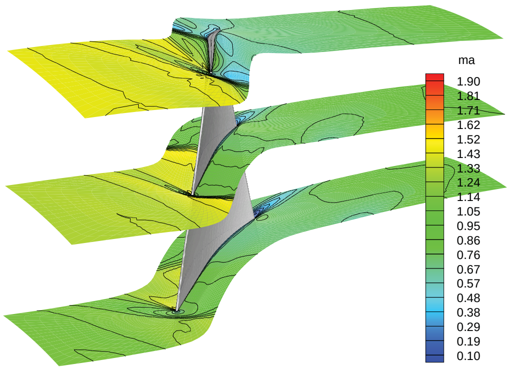

Figure 4: Relative Mach number contours on three ζ cross-sections at near-peak efficiency condition.

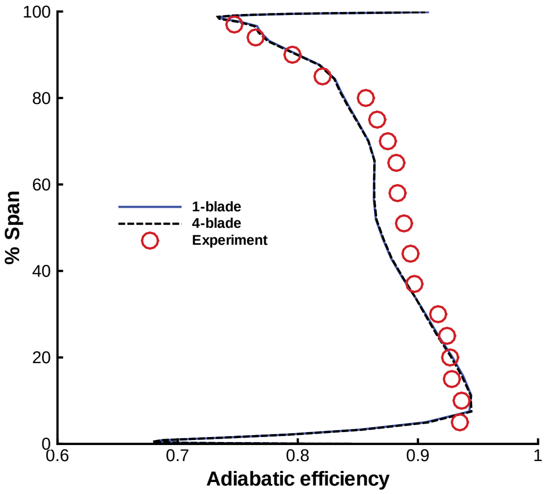

Figure 5: Spanwise distributions of adiabatic efficiency at near-peak efficiency condition.

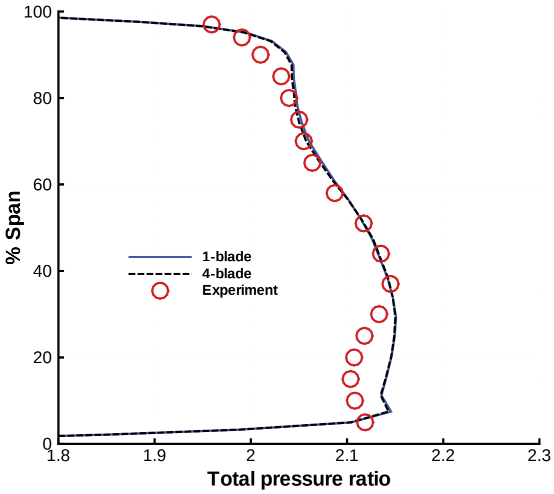

Figure 6: Spanwise distributions of total pressure ratio at near-peak efficiency condition.

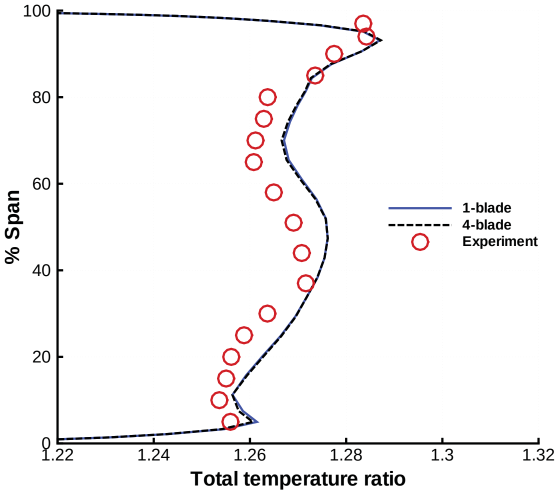

Figure 7: Spanwise distributions of total temperature ratio at near-peak efficiency condition.

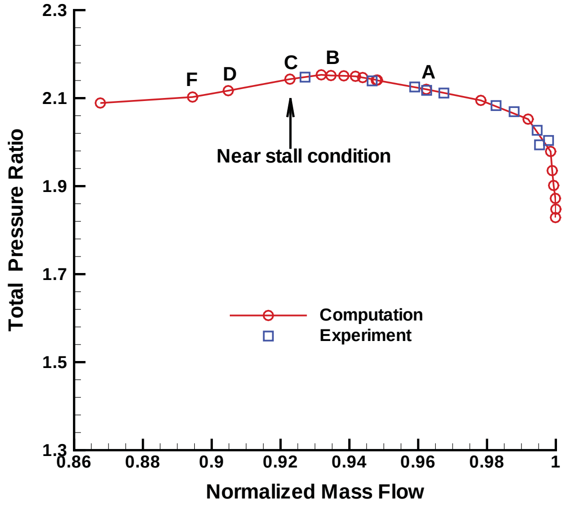

Figure 8: Overall performance: total pressure ratio vs. normalized mass flow.

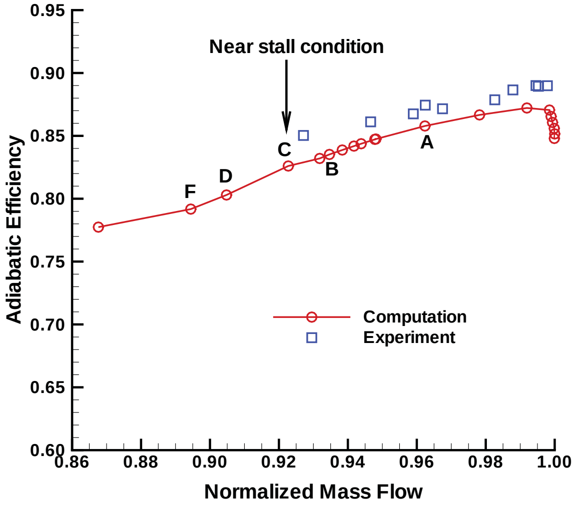

Figure 9: Overall performance: Adiabatic efficiency vs. normalized mass flow.

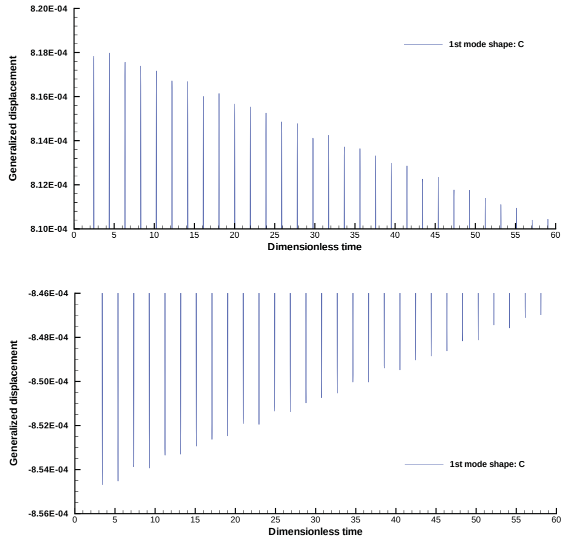

Figure 10: Time history of the generalized displacement of first mode at condition C - Damped response.

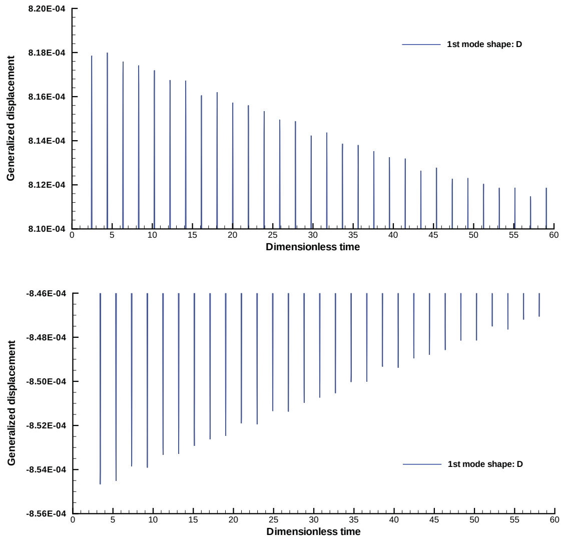

Figure 11: Time history of the generalized displacement of first mode at condition D - critical point.

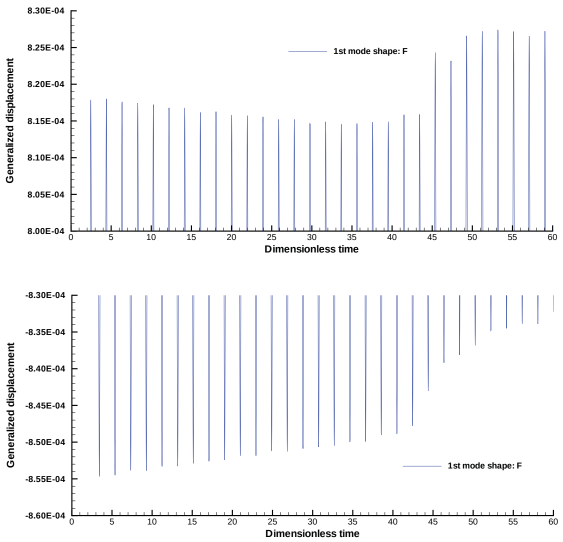

Figure 12: Time history of the generalized displacement of first mode at condition F - Diverging response.

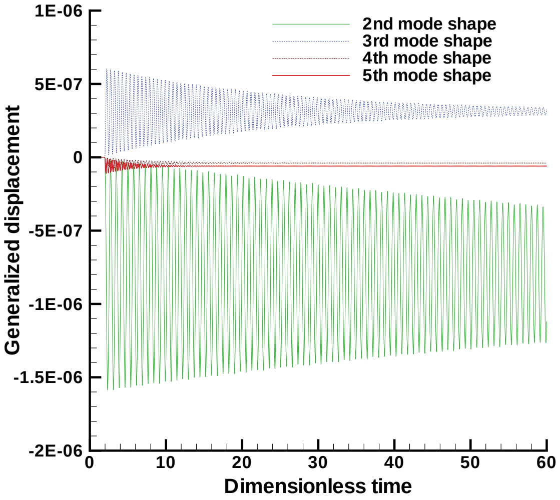

Figure 13: Time histores of the generalized displacements of 2nd - 5th modes at condition C - Damped response.

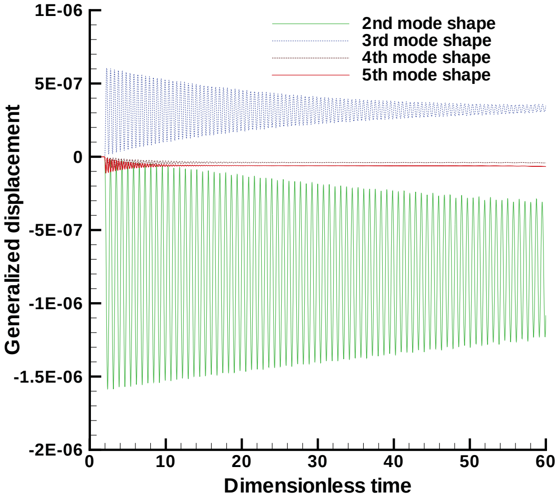

Figure 14: Time histores of the generalized displacements of 2nd - 5th modes at condition D - critical point.

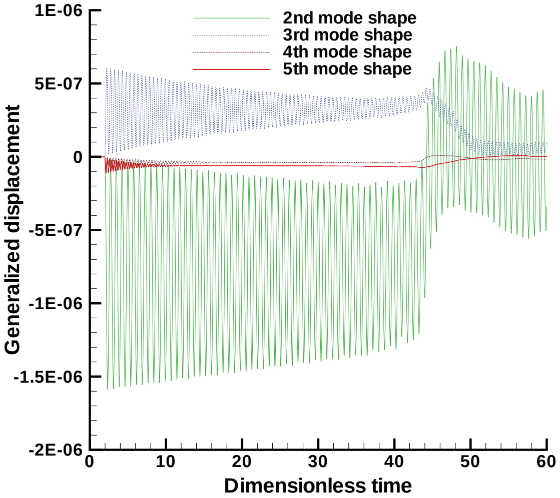

Figure 15: Time histores of the generalized displacements of 2nd - 5th modes at condition F - Diverging response.

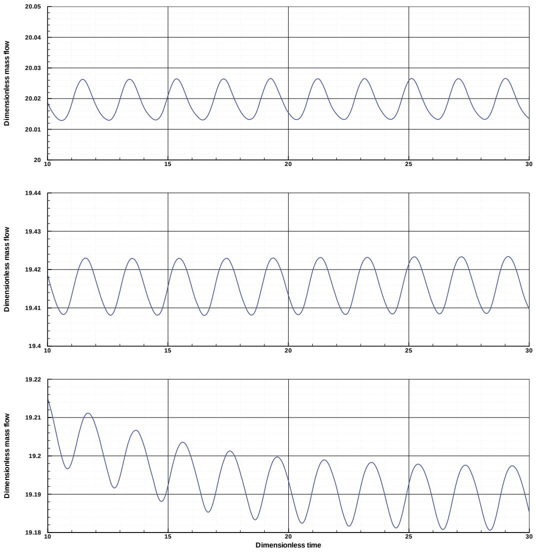

Figure 16: Time histores of the mass flows at three operating conditions A, B, and C (from upper to lower).

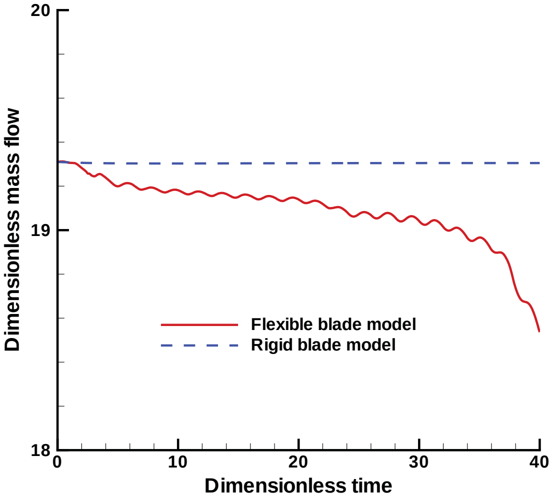

Figure 17: Time histores of the mass flows for flexible and rigid blades at condition F.